Supplementary Information:

High-Speed Graphene-based Sub−THz Receivers for 6G Wireless Communications

K. P. Soundarapandian, S. Castilla et al.

October 30, 2024

Contents

Supplementary Note 1. Devices Fabrication

Raman characterization of hBN encapsulated graphene

The optical image of the hBN/Gr/hBN stack used in the PCB-hBN receiver (D6) with a filter is shown in Supplementary Fig. 1a. Supplementary Fig. 1b shows the spatial map of the full-width-half-maxima (FWHM) of the 2D peak (Γ_{2D}), in the region marked with the dotted white line in Supplementary Fig. 1a. This map highlights the region with large Γ_{2D} ($\sim$>20 cm^{-1}) originating near the cracks/edges and folds indicating strain[1] within the graphene region, where the white space indicates the region without graphene. This map is particularly crucial for selecting the region of interest for the receiver fabrication. The histogram of Γ_{2D} over the scanned region is shown in Supplementary Fig. 1c, where the mean Γ_{2D} of $\sim$16.5 cm^{-1} indicating the high quality of the sample[2]. Supplementary Fig. 1d depicts the scatter plot of the position of the 2D (ω_{2D}) with respect to the position of the G peak (ω_G), and the data points clustered at $\sim$1582 and $\sim$2682 cm^{-1}, indicating minimal doping and strain[3]. The narrow and uniform spatial distribution of Γ_{2D} as shown in Supplementary Fig. 1c and d, Small scattered regions of the ω_{2D} and ω_G data points from Supplementary Fig. 1d suggests the ultra-high quality of the encapsulated graphene; hence, high electrical performance could be expected[4].

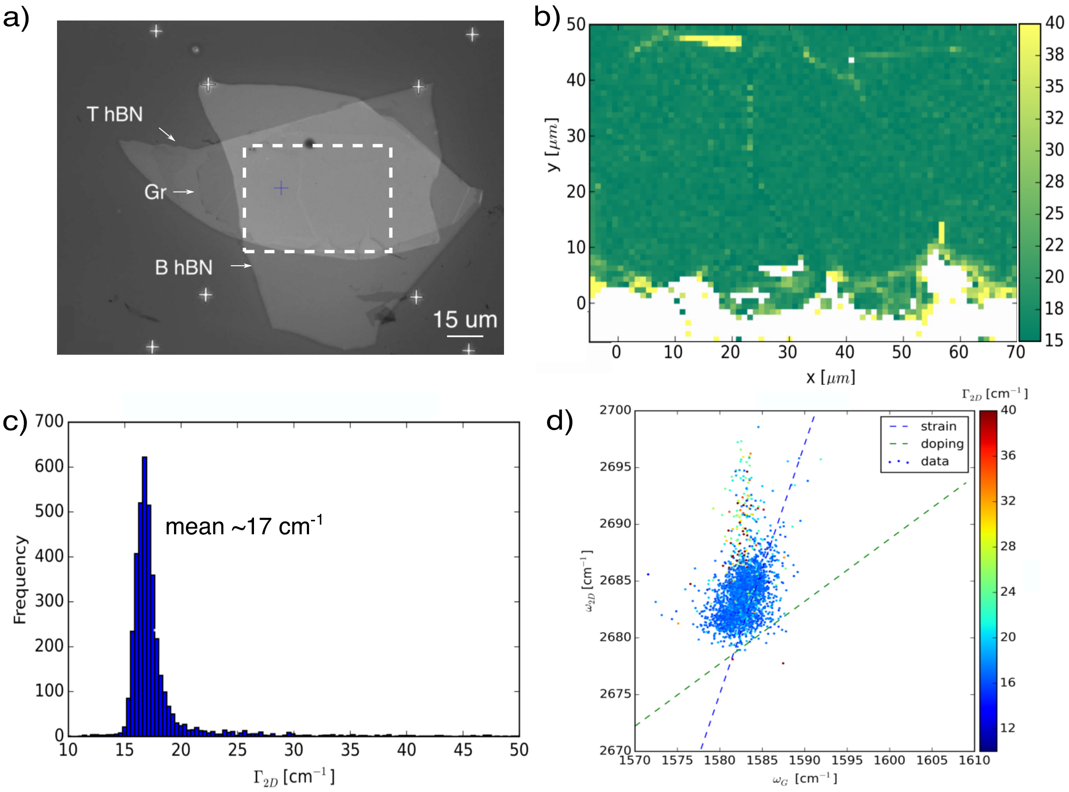

Supplementary Figure 1: Raman characterization of the PCB-hBN (D6) stack. a) optical picture of hBN/Gr/hBN stacks on a highly resistive substrate obtained with filters. b) Spatial map of Γ_{2D} scanned in the area marked with a white dotted rectangle in panel a. c) represents the histogram of Γ_{2D} with a mean value of $\sim$16.5 cm^{-1}. d) scatter plot taken in the same region as indicated in imagea, indicating low doping and strain profiles

Raman characterization of CVD Graphene

An area of 30 × 17 μm^2 was scanned, as shown as the white dotted rectangle in the Supplementary Fig. 2a, and the map Γ_{2D} of the scanned region is plotted in the Supplementary Fig. 2b. The mean Γ_{2D} was determined to be $\sim$33.7 cm^{-1}, which is on par with the literature[5,6]. Supplementary Fig. 2c reveals the scatter plot in which the ω_{2D} is plotted as a function of the ω_G, where the data points follow a slope of 2.2, as indicated by the blue dotted lines. However, the mean positions of the 2D and G peaks ($\sim$2685 cm^{-1} and $\sim$1590 cm^{-1}) are shifted with respect to the intrinsic graphene (intersection point of the blue dotted and green dotted lines), representing a strain and doping of $\sim$200 meV[7], could be resulted from the wet transfer process[5].

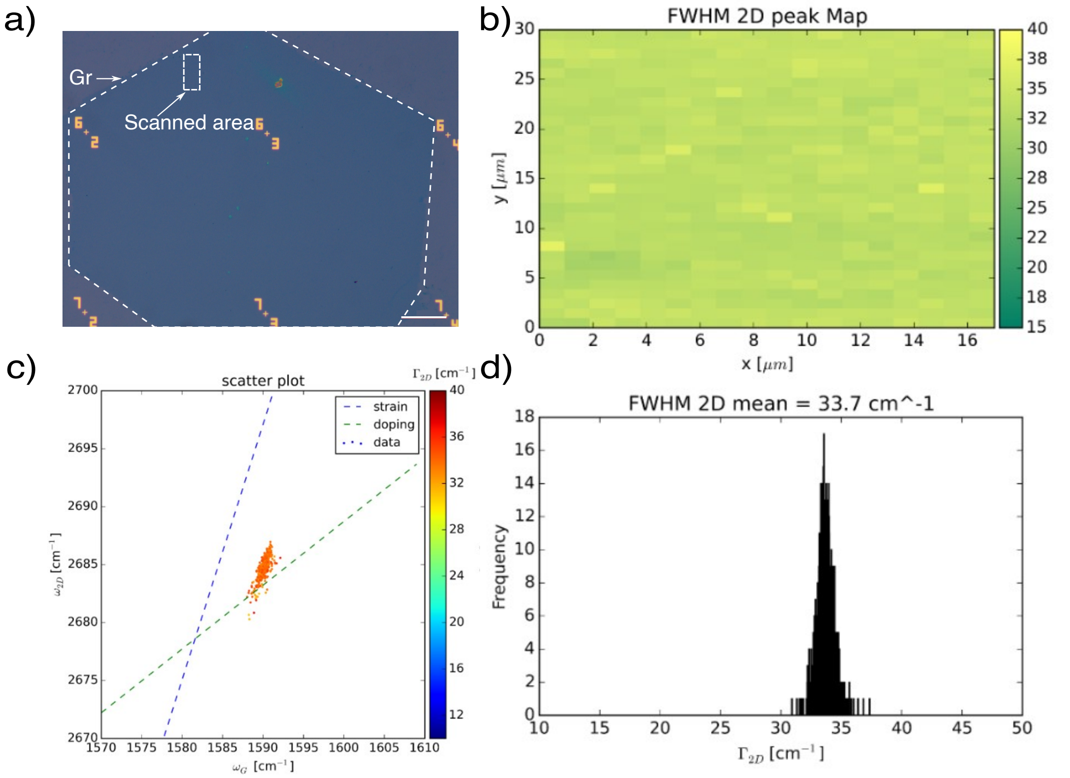

Supplementary Figure 2: Raman characterization of the CVD graphene. a) optical picture of wet transferred single crystalline CVD graphene on a highly resistive substrate, where the white dotted region highlights the area of the graphene for better visualization. Scale bar here is 30 μm. b) Spatial map of Γ_{2D} scanned in the area marked with a white dotted rectangle in image a. c) shows the scatter plot taken in the same region as indicated in image a. d) histogram of Γ_{2D} with a mean value of $\sim$33.7 cm^{-1}.

Fabrication of PCB-hBN Receiver (D6)

Supplementary Fig. 3a presents an optical image of the hBN/Gr/hBN stack captured using an optical filter, facilitating meticulous examination of the heterostructures for the presence of bubbles, contamination, and identification of the clean graphene area. Here the top and the bottom hBN are marked as T hBN and B hBN respectively, and a "+" marker is placed where a darker contrast is observed indicating the presence of Gr. By taking this and Raman maps (Supplementary Fig. 3b) as a reference, the SD electrodes is patterned, and as shown in Supplementary Fig. 3b confirms the clean channel region avoiding the bubble located in proximity. The inset of Supplementary Fig. 3c corresponds to the optical image of the device after isolation, and Supplementary Fig. 3c after dropping the dielectric hBN (denoted as D hBN). Several bubbles were entrapped along the SD electrodes, marked as traps in Supplementary Fig. 3c, which is attributed to the difference in height between the electrodes and top hBN layer. Finally, Supplementary Fig. 3d illustrates the patterned dipole antenna, 30 μm wide and 300 μm long of each branch, with a gap of $\sim$500 nm. For the WSe$_2$- hBN receivers, the B hBN is replaced with a WSe_2 flake.

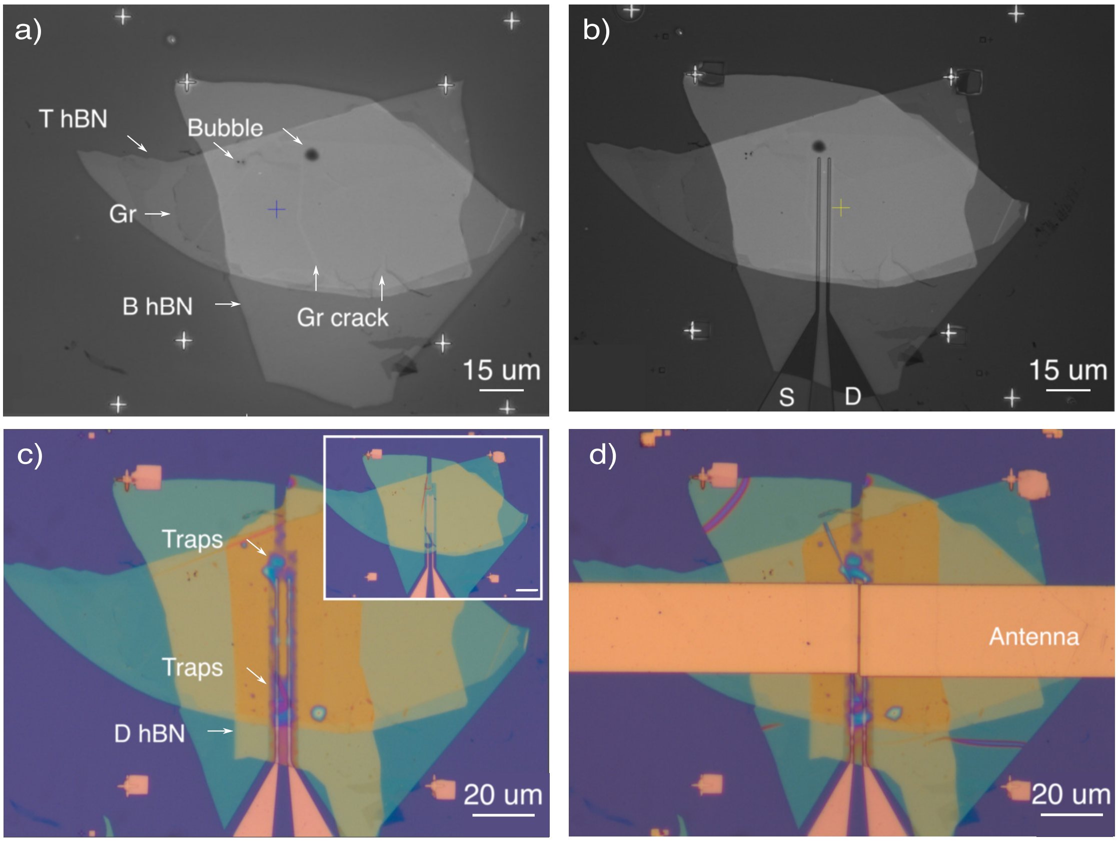

Supplementary Figure 3: Optical microscope images of the fabrication. a) and b) optical images of hBN/Gr/hBN stacks on a highly-resistive substrate obtained with filters to investigate the impurities and select the desired area to fabricate receiver. b) optical image obtained after patterning SD electrodes. c) optical image of the receiver after the dropping D hBN, and the insert shows the optical image of the electrically contacted and isolated receiver before dropping the dielectric hBN (D hBN). d) optical image of the final receiver after patterning of the dipole antenna.

Fabrication of CVD-alumina (D2) and CVD-hBN (D3 and D4) receivers

Supplementary Fig. 4 displays optical images captured at different stages throughout the fabrication process of the CVD-alumina and CVD-hBN receiver. a) optical picture of an SLG hexagon on a SiO_2/Si substrate, and white dotted lines are drawn for better visualization. b) defined SD contacts within the graphene area (dotted lines) that were etched to form an H-shape channel. c) and d) are the optical images of the fabricated CVD and hybrid receiver with Al2O3 and D hBN as dielectrics with a 30 μm wide and 600 μm long antenna, separated by a 500 nm gap on top.

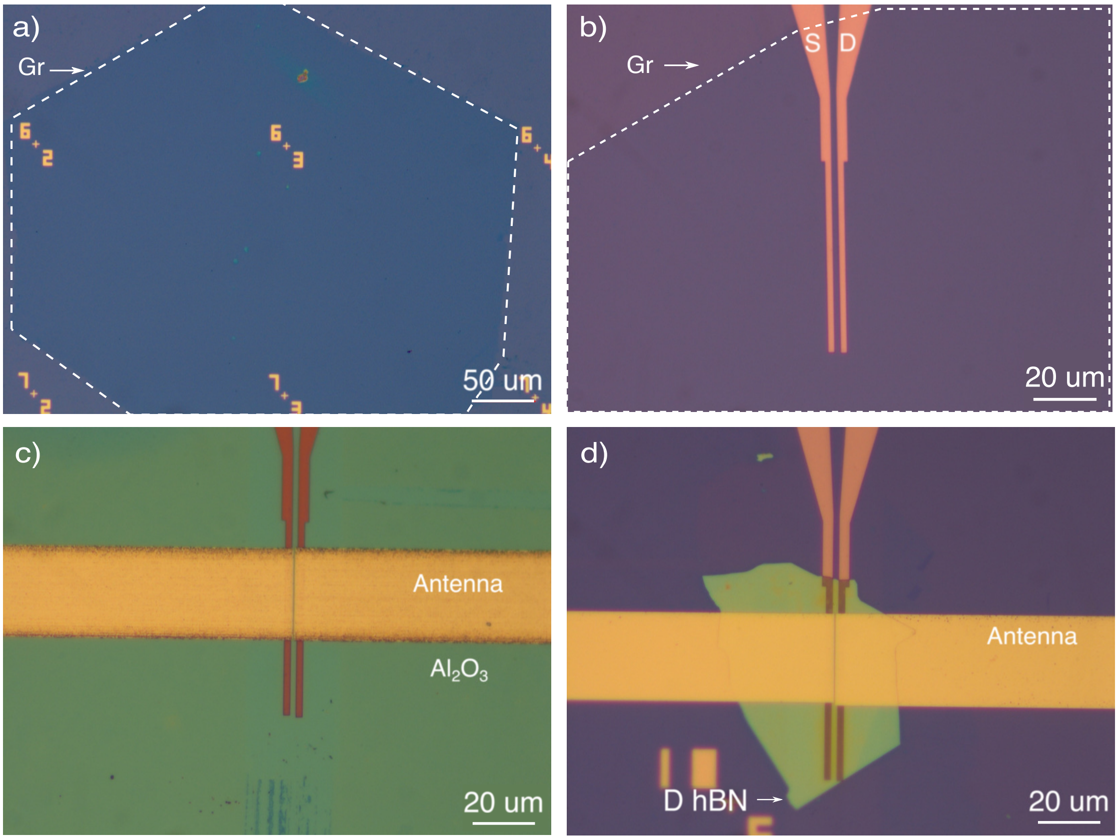

Supplementary Figure 4: Optical images of the CVD-alumina and CVD-hBN receivers. a) depicts the single-crystalline CVD graphene on a highly resistive substrate. b) H-shape patterned, isolated, and electrically contacted receiver channels. c) optical image of the fabricated CVD receiver with Al_2O_3. d) Optical image of the fabricated Hybrid receiver with D hBN isolating the receiver channel and dipole antenna.

Supplementary Note 2. Electrical Characterization

The fabricated receivers (Exfo - hBN (D1), CVD - alumina (D2), CVD - hBN (D3), WSe_2 - hBN (D5), and PCB - hBN (D6)) were first subjected to electrostatic gating, as shown in Supplementary Fig. 5 (a-e). However, the receivers function as two-terminal field-effect transistors (FET) with only S-D connections with lengths and widths of 2 and 30 μm (80 μm for the CVD receiver), where the dipole antennas act as the gate. Consequently, a bias voltage was introduced between the S-D electrodes, and the resulting alteration in current was observed while tuning the gate voltage at both antennas. Consequently, we obtained the resistance of the device with respect to the gate voltage. Hence, a model from Ref[8] was employed to fit R using the following equation:

$$R = R_c + \frac{L}{W}(\mu e n)^{-1}. \tag{1}$$

In this equation, R_c represents the contact resistance, L is the channel length, W is the channel width, μ is the mobility, e is the elementary charge, and the carrier density (n) is defined as

$$n = \sqrt{((n^*)^2 + (\beta(V_{\text{BG-}})V_{\text{CNP}})^2)}, \tag{2}$$

where, n^* represents the residual doping concentration, V_{BG} is the gate voltage, V_{CNP} is the gate voltage corresponding to the Dirac point.

$$\beta = \frac{C_{\text{ox}}}{e} = \frac{\varepsilon_0 \varepsilon_{\text{ox}}}{t_{\text{ox}} e}, \tag{3}$$

where ε_0 is the vacuum permittivity, ε_{ox} is the dielectric constant of the respective oxide/dielectric layer, and t_{ox} is the thickness of the oxide/dielectric layer. Using the equation 1, the resistance of the corresponding devices underwent fitting, as illustrated in Supplementary Fig. 5 (a-e). Subsequently, the mobility and n^* of the receivers were estimated, and the results are summarized in the table 1 in the following section.

Summary

Type (Supplementary Fig. 5)	Mobility (hole) (cm^2/Vs)	Mobility (electron) (cm^2/Vs)	n^* (cm^{-2})	Dielectric - Thickness (nm)	Substrate - Thickness (nm)	Graphene
Exfo-hBN (D1)	~ 6100	~ 12500	$\sim 3.25 \times 10^{11}$	hBN - $\sim$70	hBN - $\sim$30	Exfoliated
CVD-alumina (D2)	~ 4200	NA	$\sim 7.7 \times 10^{11}$	Al_2O_3 - $\sim$40	SiO_2 - 300	CVD
CVD-hBN (D3)	~ 1500	~ 3000	$\sim 8.3 \times 10^{11}$	hBN - $\sim$40	SiO_2 - 300	CVD
WSe_2-hBN (D5)	~ 2000	~ 2400	$\sim 6.7 \times 10^{11}$	hBN - $\sim$70	WSe_2 - $\sim$20	CVD
PCB-hBN (D6)	~ 7200	$\sim 19,000$	$\sim 2.7 \times 10^{11}$	hBN - $\sim$70	hBN - $\sim$30	Exfoliated

Supplementary Table 1: Summary of mobility and n^* for the different types of receivers.

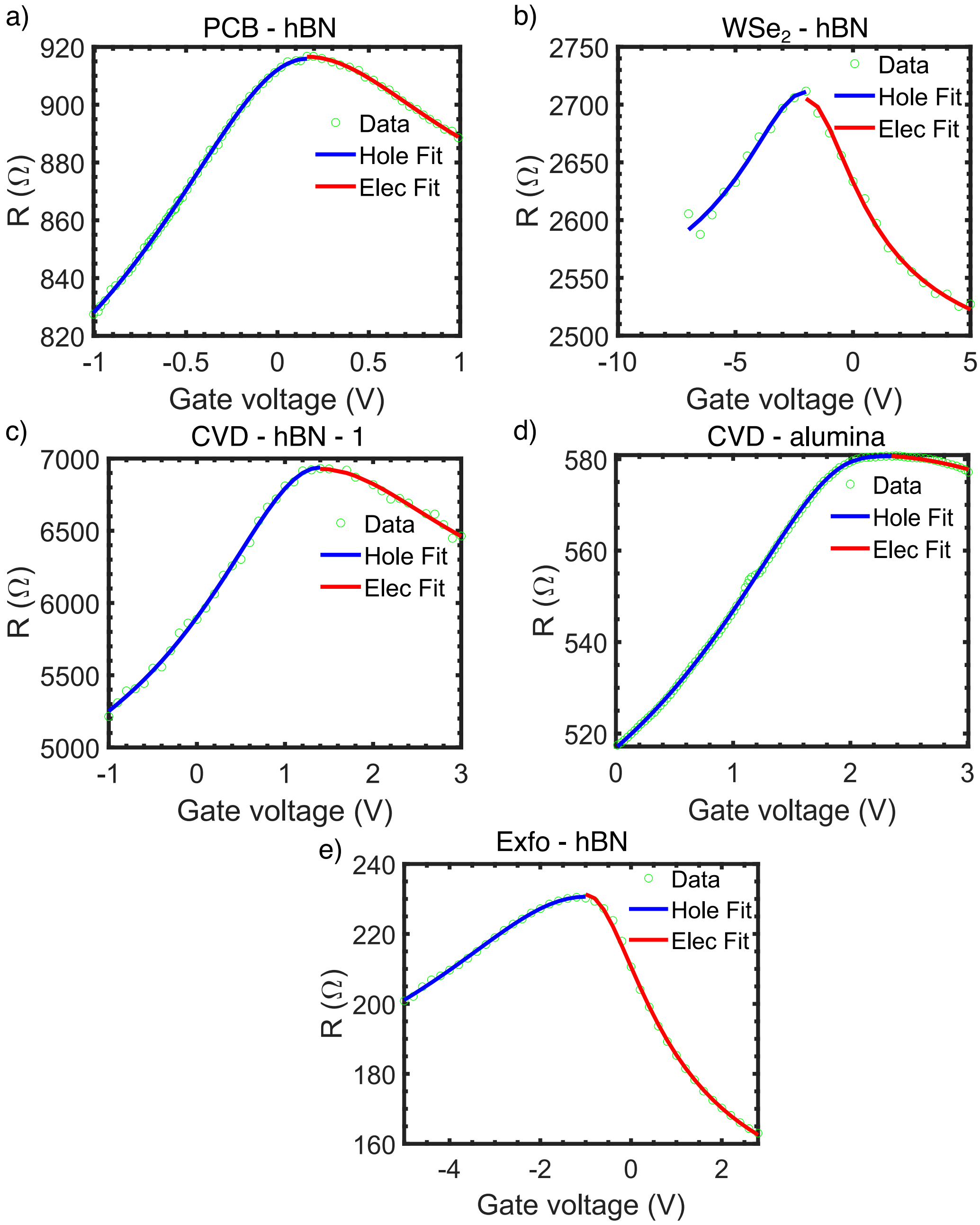

Supplementary Figure 5: Transport characteristics of fabricated receivers. (a, b, c, d and e) measured resistances (green circles) versus the backgate voltages of the PCB - hBN, WSe$_2$ - hBN, CVD - hBN-1, CVD - alumina, respectively, where the gate voltage was applied simultaneously through both sides of the dipole antenna. The resistance was fitted on both the sides of the electron (red) and holes (blue) to extract mobility and n*.

Supplementary Note 3. Opto-electronical characterization

Supplementary Fig. 6 a) and b) normalized photovoltage, mapped by sweeping the voltage applied to the gate electrodes while having zero-bias between the source and drain electrodes. The sign reversal pattern of the photoresponse shown in Supplementary Fig. 6 is a fingerprint of the PTE effect and is considered to be proof of its dominance over other photoconversion mechanisms at zero bias[9,10].

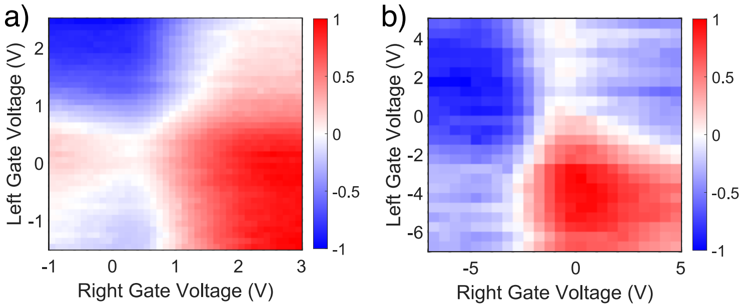

Supplementary Figure 6: Normalized photovoltage map as a function of the right and left gate voltages of the fabricated receivers. Here a) and b) are of the CVD - Alumina and WSe_2 - hBN receivers, respectively.

Supplementary Note 4. Measurement Setup

Spectral Measurement (SM)

The experimental setup used to perform the SM is outlined in Supplementary Fig. 7 . The photomixing technique used to generate the signal in the sub-THz frequency region requires that two lasers (Laser 1 and Laser 2 in Supplementary Fig. 7) at different frequencies f1 and f2 are combined through a fiber coupler, amplified by an Erbium Doped Fiber Amplifier (EDFA) and sent at the input of a high-speed photodetector, the uni-travelling carrier photodiode (UTC-PD)[11]. An electrical signal at the beating frequency f1 − f2 is generated at the output of the UTC-PD and used to feed a horn antenna after that electrical amplification is performed by a waveguide electrical amplifier. A variable optical attenuator (VOA) is used to control the optical power at the UTC-PD input. Given the polarization dependence of the responsivity of the UTC-PD (PDR in the range 2.5 dB - 4.5dB) a polarization controller is used to maximize the responsivity of the device.

The graphene receiver (GR), converts the sub-THz signal from the horn antenna into a DC signal. In this setup, a Lock-in amplifier is used to read the output of the GR, therefore, low frequency amplitude modulation of the sub-THz signal is necessary. To this end, Laser 2 is externally modulated by an Acousto-Optic Modulator (AOM) driven by an Arbitrary Waveform Generator (AWG) that also provides the reference for the Lock-In Amplifier. The amplitude modulated Laser 2 is frequency-shifted from the optical frequency to the sub-THz frequency by the photomixing block of the setup. The optical amplifier (BOA) at the AOM input is used to equalize the power of the two lasers, given the different output power of Laser 1 and Laser 2. The polarization controller and the polarizing beam splitter are needed at the input of the 3dB coupler because the output fiber of the AOM is not polarization maintaining.

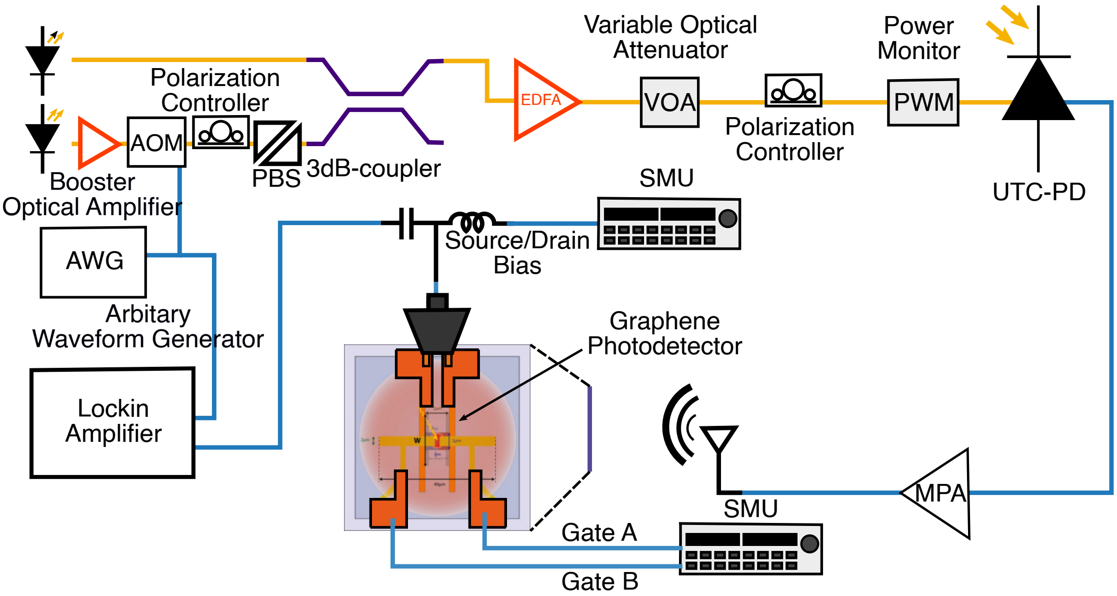

Supplementary Figure 7: Schematic representation of the experimental setup used for the SM measurements.

Bandwidth Measurement

The experimental setup, shown in Supplementary Fig. 8, is similar to the setup used for SM. The Acousto-Optic Modulator and the Arbitrary Waveform Generator are replaced by a Mach-Zehnder Modulator (MZM) and by a frequency synthesizer (Synth.), respectively, for high-speed amplitude modulation of the optical signal. The frequency synthesizer can generate a sinusoidal electrical signal up to 40 GHz to drive the MZM. The optical signal at the output of the MZM is a sinusoidal amplitude modulated signal with the same frequency of the Frequency Synth. signal. The optical-to-THz conversion is performed as in the SM experiment and the related setup block (from the 3dB-coupler to the horn antenna in Supplementary Fig. 7) is unchanged with respect to the previous experiment. The Lock-in amplifier is replaced by an Electrical Spectrum Analyzer (ESA) to read the spectrum of the electrical signal generated by the graphene receiver, i.e., to measure the intensity of sinusoidal signal at the detector output, at the same frequency of the synth. signal.

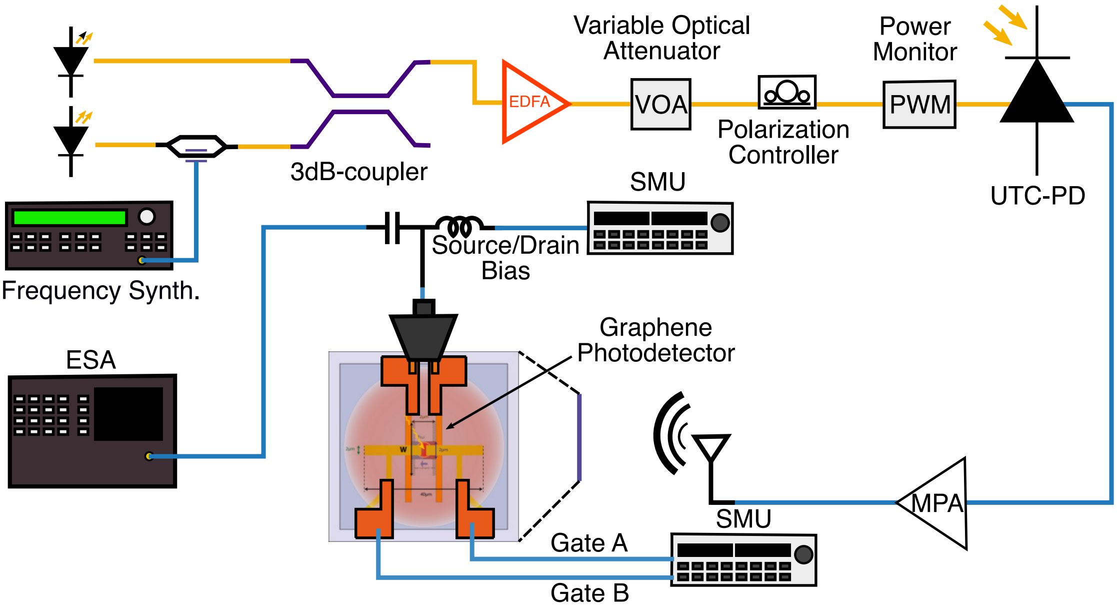

Supplementary Figure 8: Schematic representation of the experimental setup used for the bandwidth measurements

Wireless Measurement

The experimental setup for data detection is similar to that used in the previous measurement. An amplitude modulated (Non-Return-To-Zero On-Off-Keying, NRZ OOK) optical signal is down-converted from optical to sub-THz domain (carrier frequency equal to 209 GHz) by means of the photomixing block of the setup (i.e., the 3dB-coupler and the Uni-Travelling Carrier Photodiode UTC-PD). The electrical signal at the output of the UTC-PD is amplified and used to feed a horn antenna. Here, some important differences are highlighted: i) two Polymethylpentene (TPX) lenses were used for collimation and focusing of the sub-THz radiation from the horn antenna, ii) the distance between the transmitter and the device was varied in the range 0.5m-2.5m.

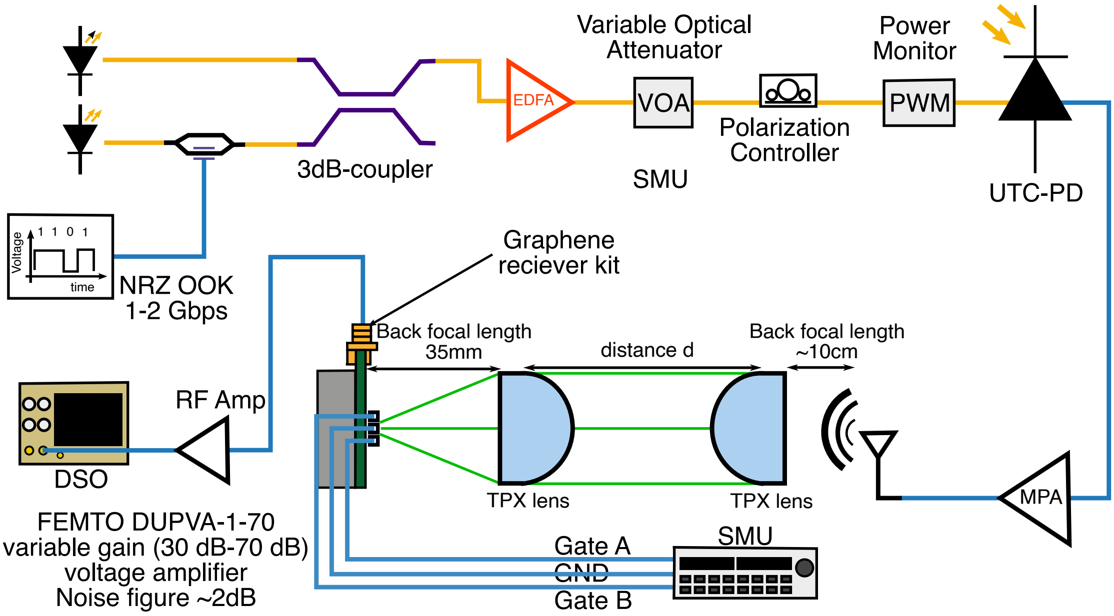

Supplementary Figure 9: Schematic representation of the experimental setup used for the Wireless measurements.

Supplementary Note 5. Data stream detection with D1

Amplifier Gain Dependence

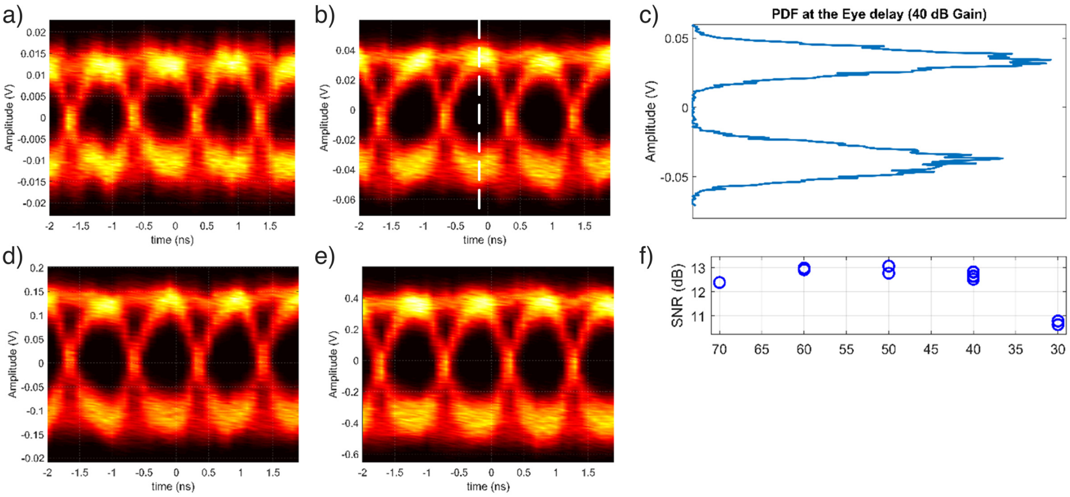

Supplementary Figure 10: Measured eye diagrams for NRZ OOK data streams at 1 Gbits^{-1} for different amplifier gains, a) 30 dB, b) 40 dB, d) 50 dB and e) 60 dB at 0.213 THz. f) Histograms of the occurrences of the amplitude voltage values at the Eye Delay (i.e., the dashed white line cut in Supplementary Fig. 10b. SNR (blue circles) extracted from the eye diagrams as a function of the amplifier gain.

Power Dependence

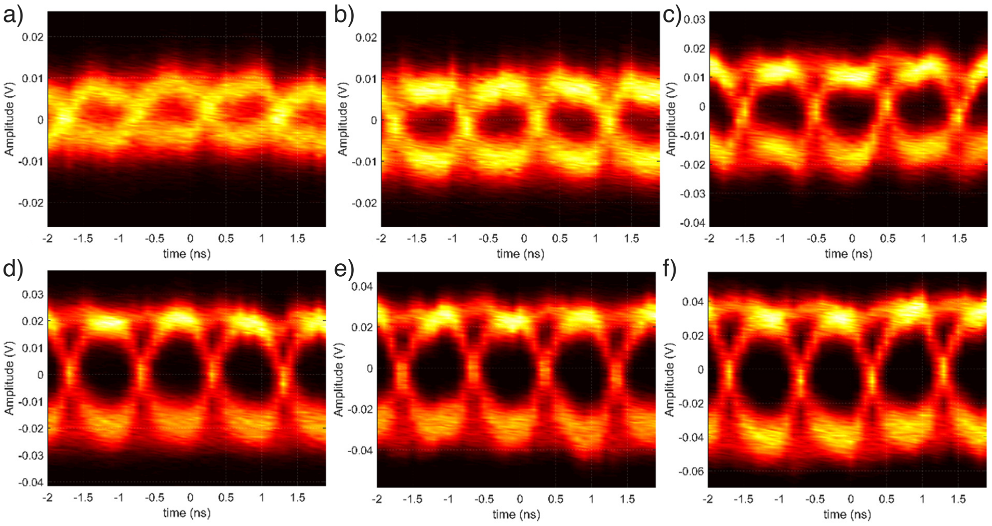

Supplementary Figure 11: Measured eye diagrams for NRZ OOK data streams at 1 Gbits^{-1} for the power measured at the output of the MPA amplifier at 0.213 THz. (a-f) are the collected eye diagrams (1 Gbits^{-1}) for different output power at the output of the MPA amplifier from (2-12.5 dBm).

Bit Rate Dependence

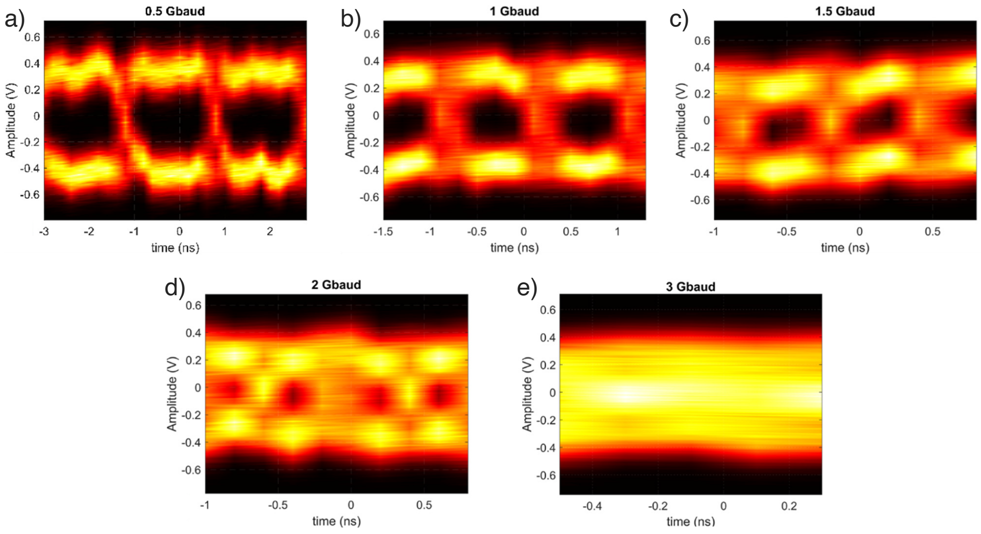

Supplementary Figure 12: Collected Eye diagrams at different bit rates with an amplifier gain of 60 dB at 0.213 THz (a-e) measured eye diagrams from 0.5 Gbits^{-1} to 3 Gbits^{-1}, respectively.

Supplementary Note 6. Evaluation kit device (D6)

PCB Design

The PCB have been realized by an European manufacturer on a 0.5 mm thick RO4350B laminate substrate (RO4350B™ Laminates - Rogers Corporation). In Supplementary Fig. 13a, the main parts of the evaluation board are shown: the graphene receiver (GR) chip realized on an intrinsic Si substrate which is in the centre of the PCB, the DC pin header on the right, and an SMA connector at the bottom of the Supplementary Fig. 13. The GR chip is connected to the PCB pads through wire bonding. A microstrip transmission line, designed to have a characteristic impedance of 50 Ω, is used to connect the RF signal bond pad to the SMA connector. The ground plane on the top metal layer is placed at a distance larger than 1.2 mm from the microstrip line. The antenna/gate electrodes on the chip, required to maximize the detector responsivity, are connected to the DC pin header (2.54 mm pitch) on the PCB, on the right of Supplementary Fig. 13a. The GR chip is placed in the middle of such a hole and on top of a mechanical support. This is done to match the height of the GR chip and of the PCB to optimize the wire bonding. Supplementary Fig. 13b shows the isometric view of the evaluation board (PCB). The mechanical support for PCB is a metallic holder. Such a holder has a $\sim$200 μm thick step in correspondence of the PCB hole to match the 0.5 mm thickness of the PCB and the $\sim$300 μm.

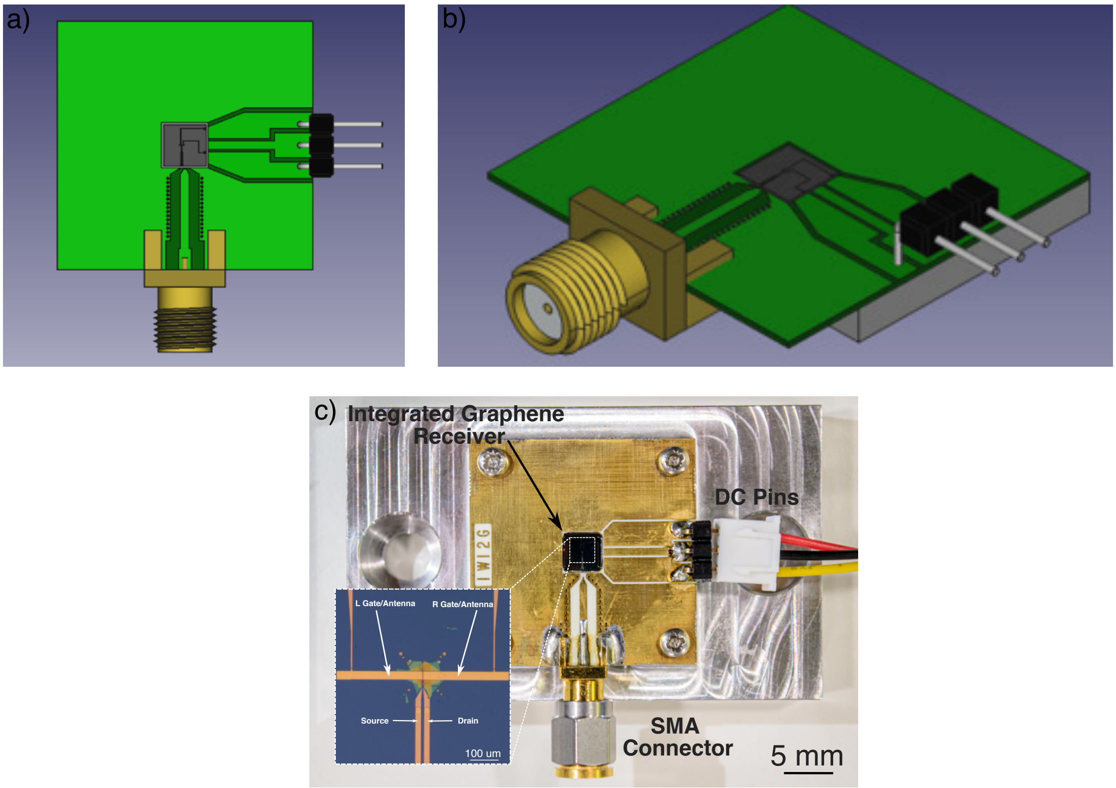

Supplementary Figure 13: Schematic representation of the fabricated PCB. a) and b) are the front and side view of the fabricated PCB-integrated hBN encapsulated graphene receiver (D6) on a metal support. c) top view picture of the entire PCB-integrated receiver. The optical picture of the receiver (D6) with antenna and S-D electrode is shown in the inset.

PCB Limited Bandwidth

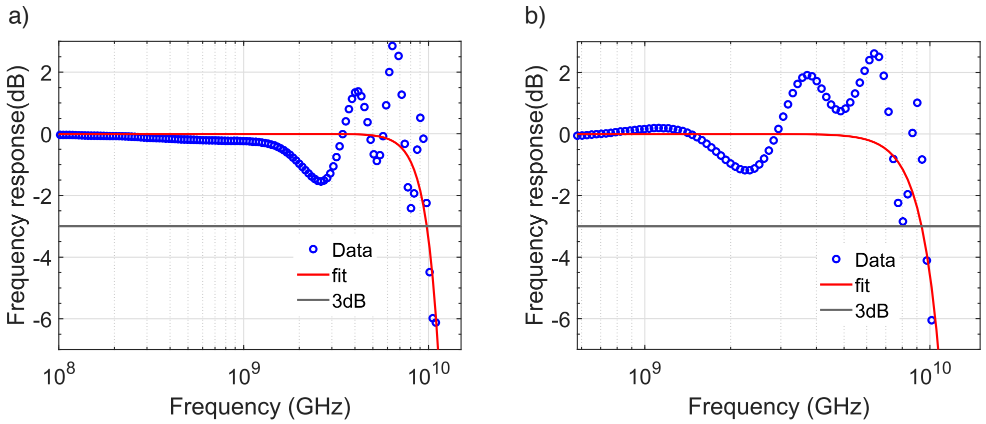

Supplementary Figure 14: Bandwidth limitation of the fabricated PCB- hBN Receiver (D6). a) Measured frequency response of the fabricated PCB with the micro-strip and without the receiver. b) Measured frequency response of the PCB-hBN receiver (D6) at 1550nm.

Data stream detection as a function of the distance (d)

The eye diagrams were collected for a distance between the transmitter and the device equal to 0.5 m, 1.5 m, and 2.5 m by changing the distance (d) between the two TPX lenses (see Supplementary Fig. 9.

Measurements at 0.5 meters

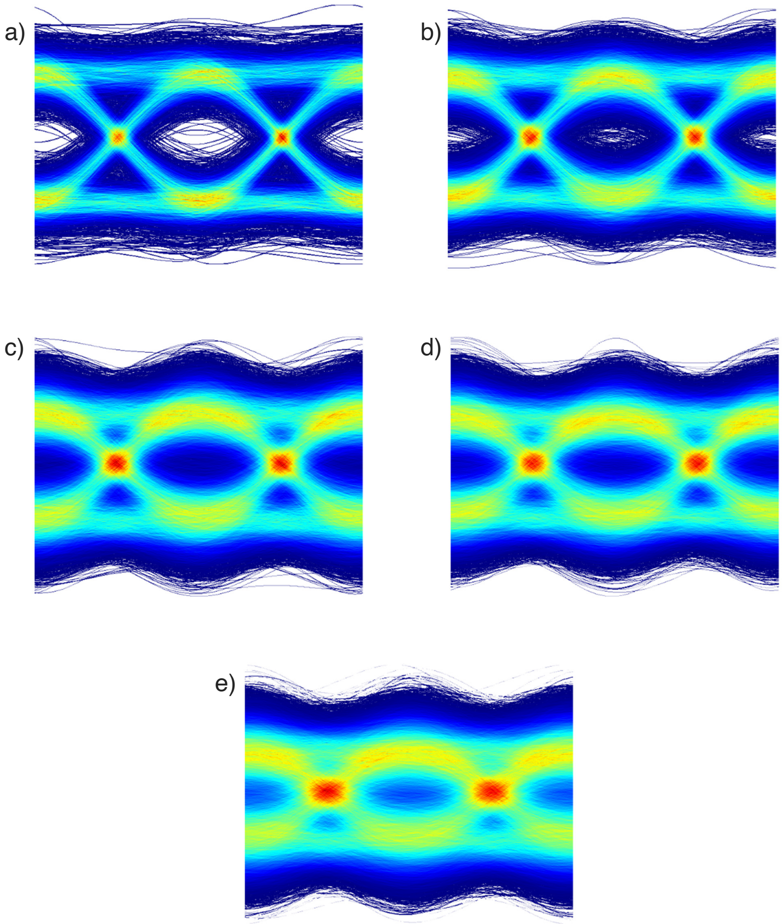

Supplementary Figure 15: Eye diagrams collected at data rates of a) 400 Mbits^{-1}, b) 1 Gbits^{-1}, c) 1.6 Gbits^{-1}, d) 2 Gbits^{-1}, and e) 3 Gbits^{-1}. Distance d equal to 0.5 m.

Measurements at 1.5 meters

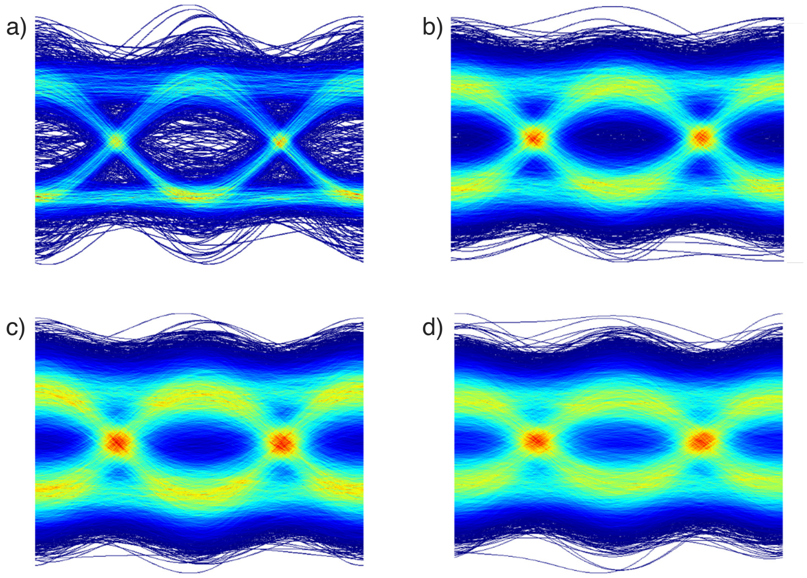

Supplementary Figure 16: Eye diagrams collected at bit rates of a) 100 Mbits^{-1}, b) 500 Mbits^{-1}, c) 800 Mbits^{-1}, and d) 1 Gbits^{-1}. Distance d equal to 1.5 m.

Measurements at 2.5 meters

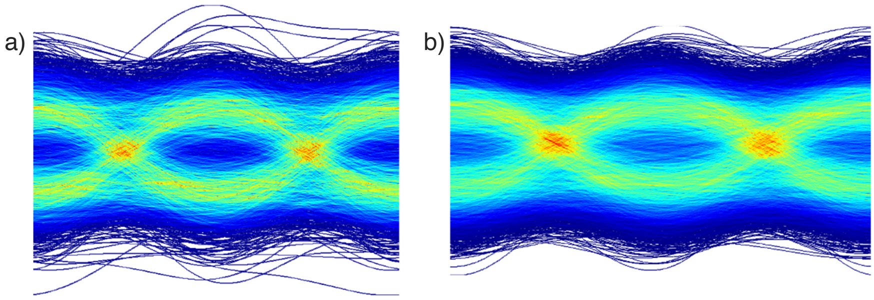

Supplementary Figure 17: Eye diagrams collected at bit rates of a) 200 Mbits^{-1} and b) 500 Mbits^{-1}. Distance d equal to 2.5 m.

Supplementary Note 7. Enhancement of graphene absorption

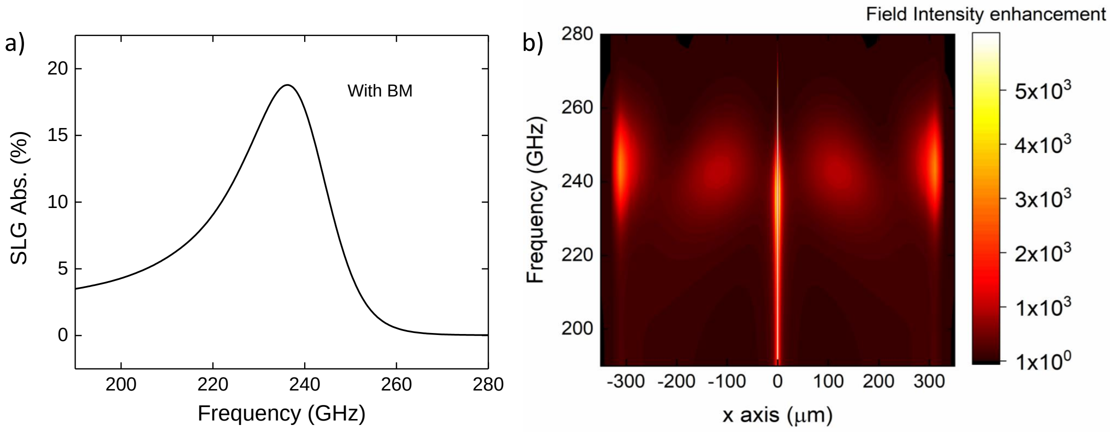

Supplementary Figure 18: Enhancement of graphene absorption. a) Absorption percentage of single layer graphene including the antenna and back mirror in D1. We achieve a maximum value of ∼20%. b) Spatial map of the field intensity enhancement across the antenna length (∼600 µm), where $x = 0$ is at the center of the antenna gap. The field-enhancement spatial map is shown for the investigated spectral range.

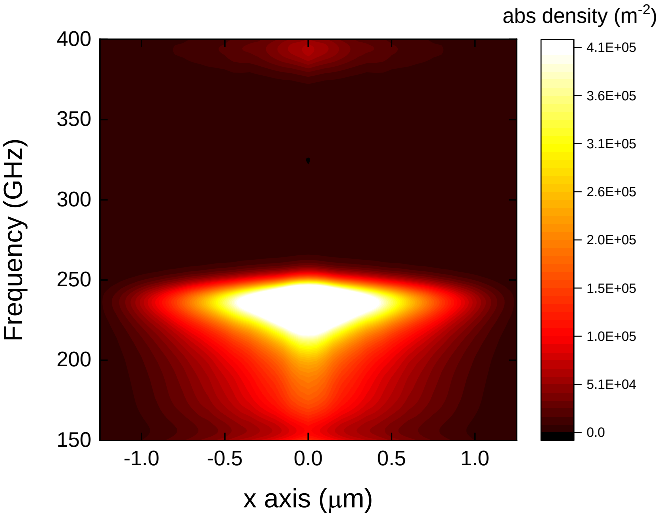

Supplementary Figure 19: Absorption density for an extended carrier frequency range across the source-drain direction in the graphene channel of D1, where $x = 0$ is at the center of the antenna gap.

Supplementary Note 8. Device responsivity

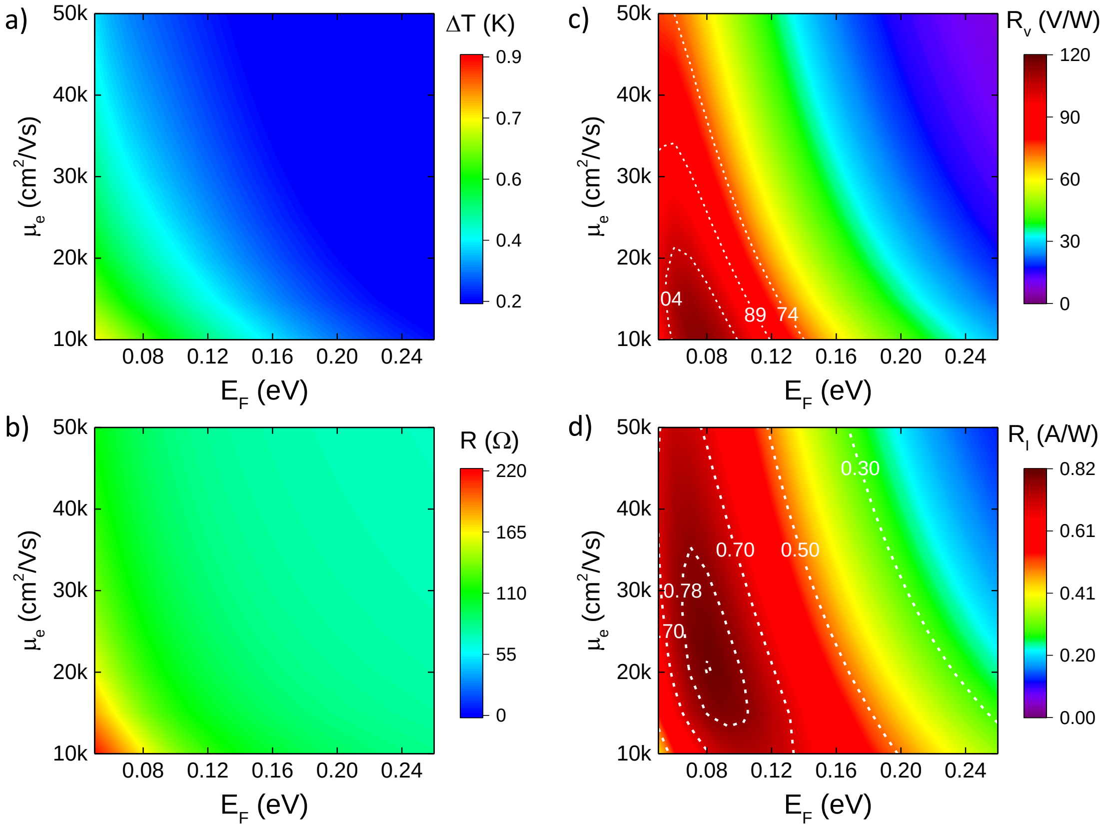

Supplementary Figure 20: Device responsivity. a) Maximum temperature rise[12] across the graphene channel as a function of the graphene mobility (y-axis) and Fermi energy (x-axis). Similar to panel a, but for b) resistance, c) internal responsivity in V/W, and d) internal responsivity in A/W. By considering the absorption percentage of ∼20%, as described in Supplementary Fig. 18a, we obtain an external responsivity of 0.164 A/W (24 V/W), which is very close to the experimental values, which correspond to 0.160 A/W (∼30 V/W) for D1.

Supplementary Note 9. Bandwidth of the receivers

The 3 dB electrical bandwidth $f_{3\mathrm{dB}}$ is obtained by fitting the measured frequency response, assuming a transfer function with a single pole, whose square modulus is given by:

$$F(\omega) = \frac{1}{1 + \omega^2 \tau^2}$$

where $\omega = 2\pi f$, $\tau = \frac{1}{2\pi f_{3\mathrm{dB}}}$, and τ is the response time, and f is the modulation frequency.

Receivers with Antenna

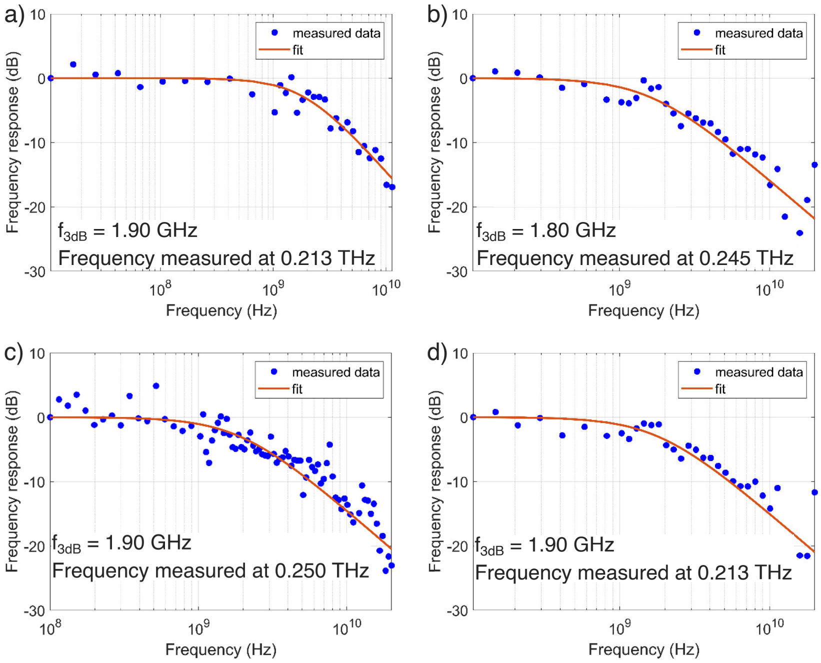

Supplementary Figure 21: Measured frequency response of the fabricated receivers with antenna. a) CVD-alumina (D2), b) CVD-hBN-1 (D3), c) CVD-hBN-2 (D4), and d) Exfo-hBN (D1) are the measured frequency response with a fit to extract the f_{3dB} bandwidth at 0.213, 0.245, 0.250, and 0.213 THz respectively.

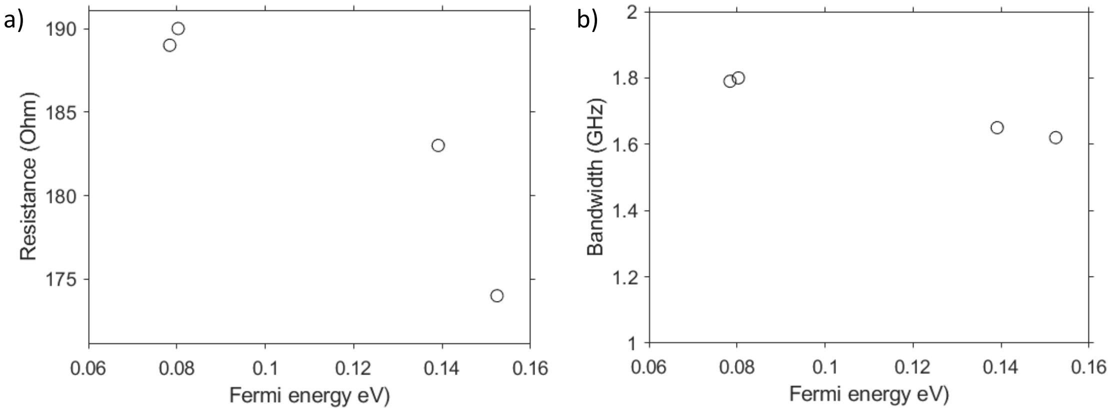

Supplementary Figure 22: Bandwidth as a function of Fermi energy in D1. a) Resistance as a function of Fermi energy. We observe the expected resistance drop when increasing the Fermi energy in graphene. b) Bandwidth as a function of Fermi energy with carrier frequency of 0.213 THz, which shows that the bandwidth decreases slightly when the Fermi energy is increased. However, the bandwidth value doesn't change significantly, which is in agreement with other measurements reported in the literature.[13]

CVD - alumina - without Antenna and back mirror (D7)

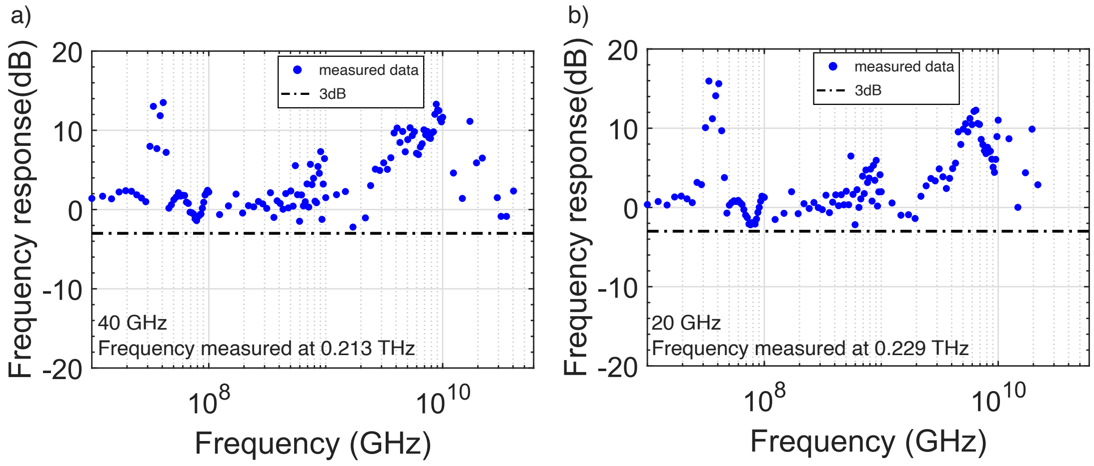

Supplementary Figure 23: Measured frequency response of the fabricated CVD - alumina receiver without antenna and back mirror (D7). a) and b) measured frequency response at 0.213 and 0.229 THz respectively with a f_{3dB} guideline. The plots suggest that there is no roll-off in the response, and the bandwidth of the receivers is only limited by low optical power and noise in the measurement setup.

Supplementary Note 10. Bandwidth limitation

We calculate the frequency response (3 dB bandwidth) by considering the parameters of the investigated devices, as shown in Supplementary Table 2. The equivalent circuit of the device is similar to that presented in ref. 14, with a 50 Ohm termination at the setup electronics (for example, ESA). RC-limited and optical-limited bandwidths are described in the main text. We note that the parallel-plate capacitor approach becomes invalid at very high frequencies. Therefore, to provide an accurate upper bound of the RC limitation, 3D RF simulations are required, which are beyond the scope of this work.

We obtain a better agreement between the experimental values and those calculated using the optical-limited bandwidth. Here, we consider a Q-factor of ∼15 (14.86), whereas for the non-resonant cases, we consider Q=1. The highest calculated and measured bandwidths, correspond to D7, which comprises a non-resonant split gate of 10 µm and a graphene channel of the same dimensions. In Supplementary Fig. 24, we plot the bandwidths of all measured devices.

Device	**Device resistance (Ω)**	**Equivalent resistance (Ω)**	**Capacitance (fF)**	**Experiment BW (GHz)**	**RC BW (GHz)**	**Optical BW (GHz)**
D1	190	39.5	57	1.8	71	4.9
D2	553	45.8	60	1.9	58	4.9
D3	2311	48.9	84	1.9	39	4.9
D7	2500	49.0	114	40	29	4400
D6 at telecom freq.	1000	47.6	31	10	106	73
D6	1000	47.6	31	0.7	106	4.9

Supplementary Table 2: Parameters to calculate the bandwidth of the sub-THz receivers

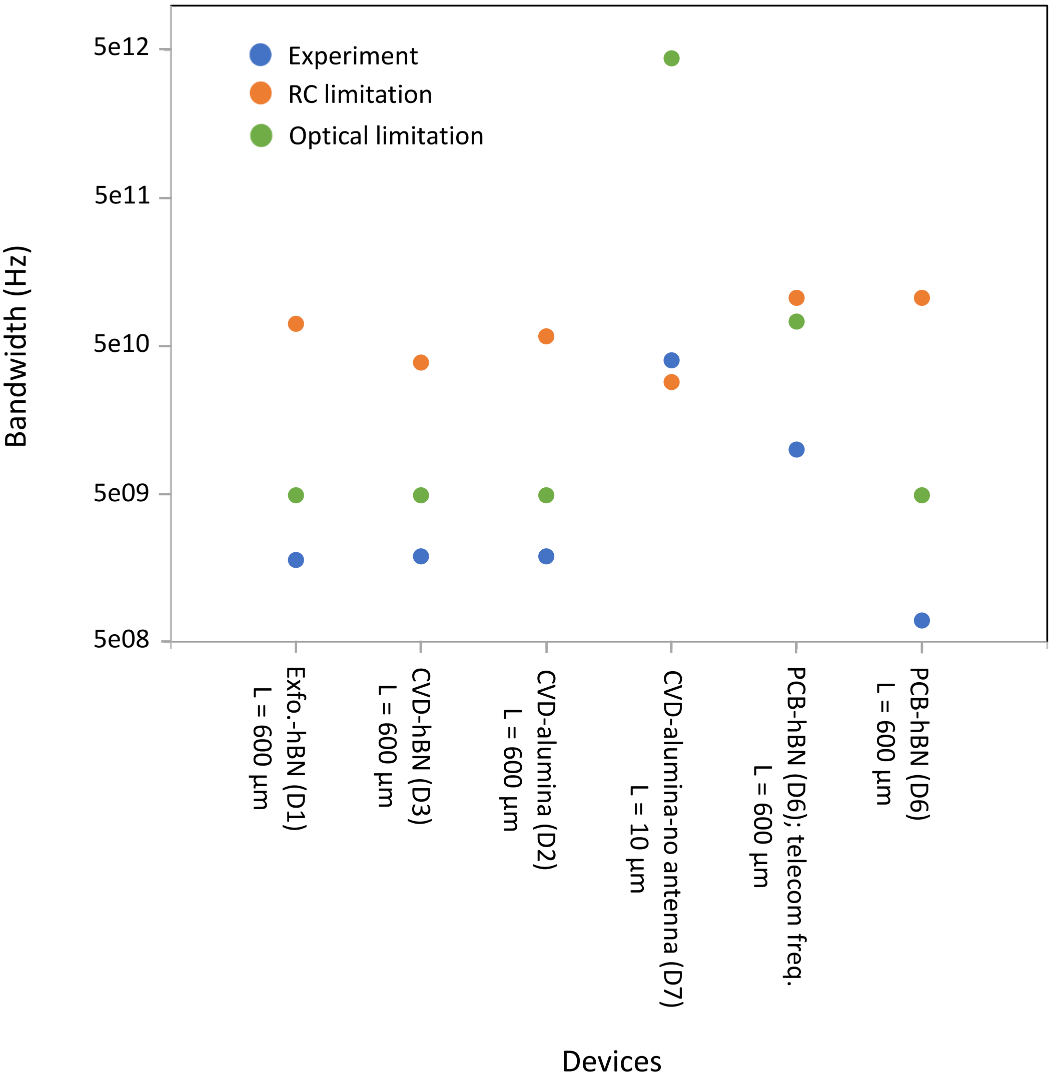

Supplementary Figure 24: Bandwidth of all the devices in log scale for the experimental data (blue), RC-limited bandwidth (orange), and for the optical limited bandwidth (green). We note that D7 has a split-gate length of 10 µm, which shows the highest experimental and optical bandwidth. We calculate the optical bandwidth by considering a Q-factor of 15 for D1, D2, D3, and D6. We assume a Q-factor of 1 for devices D6 at telecom frequency (∼190 THz) and D7.

Supplementary Note 11. Comparison with other graphene sub-THz detectors

Type/ Reference	**Mechanism**	**Bias voltage (V)**	**Frequency (THz)**	**Responsivity (V/W), (A/W)**	**NEP (nW/$\sqrt{\text{Hz}}$)**	**Rise time**	**Normalization area***	**Graphene (Footprint µm^2)**
Exf.[15]	Plasma waves	-	0.29-0.38	1.2, 0.0013	$\sim$2	-	$\lambda^2/4$	2.5×7.5
Exf.[16]	Plasma waves	-	0.3	0.15,-	$\sim$200	-	$\lambda^2/4$	10×7
CVD[17]	Resistive self-mixing	-	0.4	74,-	0.13	-	No*	2×2.5
CVD[18]	Photovoltaic	0.5	0.1-0.12	280,-	0.1	4 µs	Device area*	6×60
CVD[19]	PTE	0.1	0.1,0.14,0.3	28,-	0.35	9 µs	$\lambda^2/450$	9×4
Exf.[20]	Ballistic rectifier	-	0.1-0.69	764,-	0.034	-	$\lambda^2/4\pi$	2.5×2.5
Exf.[21]	PTE	-	0.13-0.45	20,-	0.6	-	No*	6×2.6
Exf.[22]	PTE	-	0.3	-,0.0019	0.67	-	Graphene area	31×10
CVD[23]	PTE	-	0.4	63,-	0.11	-	No*	2.7×2
CVD[24]	PTE	-	0.6	35,-	0.3	-	A_{eff}/λ^2	5×5
CVD[25]	Resistive self-mixing	-	0.6	14,-	0.515	-	No*	2×2.5
CVD[26]	Photoconductive	0.4	0.15	400,-	0.5	<20 µs	Device area*	5×60
CVD[27]	PTE	-	0.12	29,-	0.009	7 µs	Effective area	-
Exf.[28]	PTE	-	0.105	-, 1.54	0.020	900 ns	Device area*	14×5
Exf./ This work	PTE	-	0.19-28	30,0.16	0.058	194 ps	λ^2/π	30×2
CVD/ This work	PTE	-	0.19-0.28	6.9,0.013	0.95	184 ps	λ^2/π	30×2

[1] Device Area* - Including antenna and graphene. [2] No* - In this work a silicon hyper-hemispherical lens was employed. [3] Normalization area* - The normalization area, Anorm, refers to the area to which the incident power was normalized: $P_{\text{norm}} = P_{\text{in}} \times \frac{A_{\text{norm}}}{A_{\text{focus}}}$. In our work, for example, we use the power in a diffraction-limited spot $P_{\text{diff}} = P_{\text{in}} \times \frac{A_{\text{diff}}}{A_{\text{focus}}}$; i.e., we use $A_{\text{norm}} = A_{\text{diff}} = \frac{\lambda^2}{\pi}$.

Supplementary Table 3: Comparison of graphene sub-THz photodetectors

References

[1] Lee, J. E., Ahn, G., Shim, J., Lee, Y. S. & Ryu, S. Optical separation of mechanical strain from charge doping in graphene. *Nature Communications* **3**, 1–8 (2012). Number: 1 Publisher: Nature Publishing Group.

[2] Purdie, D. G. et al. Cleaning interfaces in layered materials heterostructures. *Nature Communications* **9**, 1–12 (2018). ISBN: 4146701807558 Publisher: Springer US _eprint: 1803.00912.

[3] Ferrari, A. C. & Basko, D. M. Raman spectroscopy as a versatile tool for studying the properties of graphene. *Nature Nanotech.* **8**, 235–246 (2013). Publisher: Nature Publishing Group.

[4] Couto, N. J. G. et al. Random strain fluctuations as dominant disorder source for high-quality on-substrate graphene devices. *Physical Review X* **4**, 41019 (2014). Publisher: American Physical Society _eprint: 1401.5356.

[5] Wu, Z. et al. Step-by-step monitoring of CVD-graphene during wet transfer by Raman spectroscopy. *RSC Advances* **9**, 41447–41452 (2019). Publisher: Royal Society of Chemistry.

[6] Lin, L. et al. Towards super-clean graphene. *Nature Communications* **10**, 1912 (2019). Number: 1 Publisher: Nature Publishing Group.

[7] Das, A. et al. Monitoring dopants by Raman scattering in an electrochemically top-gated graphene transistor. *Nature Nanotechnology* **3**, 210–215 (2008). Number: 4 Publisher: Nature Publishing Group.

[8] Tan, Y.-W. et al. Measurement of scattering rate and minimum conductivity in graphene. *Phys. Rev. Lett.* **99**, 246803 (2007).

[9] Gabor et al. Hot Carrier–Assisted Intrinsic Photoresponse in Graphene. *Science* **334**, 648–652 (2011).

[10] Song, J. C. W., Rudner, M. S., Marcus, C. M. & Levitov, L. S. Hot Carrier Transport and Photocurrent Response in Graphene. *Nano Lett* **11**, 4688–4692 (2011).

[11] Horst, Y. et al. Transparent Optical-THz-Optical Link at 240/192 Gbit/s Over 5/115 m Enabled by Plasmonics. *Journal of Lightwave Technology* **40**, 1690–1697 (2022). Conference Name: Journal of Lightwave Technology.

[12] Castilla, S. et al. Plasmonic antenna coupling to hyperbolic phonon-polaritons for sensitive and fast mid-infrared photodetection with graphene. *Nature Communications* **11**, 4872 (2020).

[13] Xia, F., Mueller, T., Lin, Y. M., Valdes-Garcia, A. & Avouris, P. Ultrafast graphene photodetector. *Nature Nanotechnology* **4**, 839–843 (2009). Publisher: Nature Publishing Group.

[14] Marconi, S. et al. Photo thermal effect graphene detector featuring 105 Gbit s1 NRZ and 120 Gbit s1 PAM4 direct detection. *Nature Communications* **12**, 806 (2021). Number: 1 Publisher: Nature Publishing Group.

[15] Spirito, D. et al. High performance bilayer-graphene terahertz detectors. *Applied Physics Letters* **104**, 061111 (2014).

[16] Vicarelli, L. et al. Graphene field-effect transistors as room-temperature terahertz detectors. *Nature Materials* **11**, 865–871 (2012). Number: 10 Publisher: Nature Publishing Group.

[17] Generalov, A. A., Andersson, M. A., Yang, X., Vorobiev, A. & Stake, J. A 400-ghz graphene fet detector. *IEEE Transactions on Terahertz Science and Technology* **7**, 614–616 (2017).

[18] Liu, C. et al. Towards sensitive terahertz detection via thermoelectric manipulation using graphene transistors. *NPG Asia Materials* **10**, 318–327 (2018). Publisher: Nature Publishing Group.

[19] Guo, W. et al. Graphene-based broadband terahertz detector integrated with a square-spiral antenna. *Opt. Lett.* **43**, 1647–1650 (2018).

[20] Auton, G. et al. Terahertz detection and imaging using graphene ballistic rectifiers. *Nano Letters* **17**, 7015–7020 (2017). PMID: 29016145.

[21] Bandurin, D. A. et al. Dual origin of room temperature sub-terahertz photoresponse in graphene field effect transistors. *Applied Physics Letters* **112**, 141101 (2018).

[22] Delgado-Notario, J. A. et al. Enhanced terahertz detection of multigate graphene nanostructures. *Nanophotonics* **11**, 519–529 (2022).

[23] Ludwig, F. et al. Terahertz detection with graphene fets: Photothermoelectric and resistive self-mixing contributions to the detector response. *ACS Applied Electronic Materials* **6**, 2197–2212 (2024).

[24] Joint, F. et al. Terahertz antenna impedance matched to a graphene photodetector. *ACS Applied Electronic Materials* **6**, 4819–4825 (2024).

[25] Zak, A. et al. Antenna-integrated 0.6 thz fet direct detectors based on cvd graphene. *Nano Letters* **14**, 5834–5838 (2014). PMID: 25203787.

[26] Liu, C. et al. Room-temperature photoconduction assisted by hot-carriers in graphene for sub-terahertz detection. *Carbon* **130**, 233–240 (2018).

[27] Jiang, M. et al. Monolayer Graphene Terahertz Detector Integrated with Artificial Microstructure. *Sensors* **23**, 3203 (2023). Number: 6 Publisher: Multidisciplinary Digital Publishing Institute.

[28] Hong, L. et al. Sensitive Room-Temperature Graphene Photothermoelectric Terahertz Detector Based on Asymmetric Antenna Coupling Structure. *Sensors* **23**, 3249 (2023). Number: 6 Publisher: Multidisciplinary Digital Publishing Institute.